Biomedical Optics EXPRESS

Near-infrared spectroscopic photoacoustic microscopy using a multi-color fiber laser source

Takashi Buma,[1,2,*] Benjamin C. Wilkinson,[2] and Timothy C. Sheehan[2]

[1]*Department of Electrical and Computer Engineering, Union College, Schenectady, NY 12308, USA*
[2]*Bioengineering Program, Union College, Schenectady, NY 12308, USA*
[*]*bumat@union.edu*

Abstract: We demonstrate a simple multi-wavelength optical source suitable for spectroscopic optical resolution photoacoustic microscopy (OR-PAM) of lipid-rich tissue. 1064 nm laser pulses are converted to multiple wavelengths beyond 1300 nm via nonlinear optical propagation in a birefringent optical fiber. OR-PAM experiments with lipid phantoms clearly show the expected absorption peak near 1210 nm. We believe this simple multi-color technique is a promising cost-effective approach to spectroscopic OR-PAM of lipid-rich tissue.

OCIS codes: (110.5120) Photoacoustic imaging; (190.4370) Nonlinear optics, fibers; (190.4380) Nonlinear optics, four-wave mixing; (190.5890) Scattering, stimulated.

References and links

1. K. Maslov, H. F. Zhang, S. Hu, and L. V. Wang, "Optical-resolution photoacoustic microscopy for in vivo imaging of single capillaries," Opt. Lett. **33**(9), 929–931 (2008).
2. H. F. Zhang, K. Maslov, G. Stoica, and L. V. Wang, "Functional photoacoustic microscopy for high-resolution and noninvasive in vivo imaging," Nat. Biotechnol. **24**(7), 848–851 (2006).
3. K. Jansen, M. Wu, A. F. W. van der Steen, and G. van Soest, "Photoacoustic imaging of human coronary atherosclerosis in two spectral bands," Photoacoustics **2**(1), 12–20 (2014).
4. B. Wang, A. Karpiouk, D. Yeager, J. Amirian, S. Litovsky, R. Smalling, and S. Emelianov, "Intravascular photoacoustic imaging of lipid in atherosclerotic plaques in the presence of luminal blood," Opt. Lett. **37**(7), 1244–1246 (2012).
5. T. J. Allen, A. Hall, A. P. Dhillon, J. S. Owen, and P. C. Beard, "Spectroscopic photoacoustic imaging of lipid-rich plaques in the human aorta in the 740 to 1400 nm wavelength range," J. Biomed. Opt. **17**(6), 061209 (2012).
6. P. Wang, J. R. Rajian, and J.-X. Cheng, "Spectroscopic imaging of deep tissue through photoacoustic detection of molecular vibration," J. Phys. Chem. Lett. **4**(13), 2177–2185 (2013).
7. T. P. Matthews, C. Zhang, D. K. Yao, K. Maslov, and L. V. Wang, "Label-free photoacoustic microscopy of peripheral nerves," J. Biomed. Opt. **19**(1), 016004 (2014).
8. D. Koeplinger, M. Liu, and T. Buma, "Photoacoustic microscopy with a pulsed multi-color source based on stimulated Raman scattering," *Proc. of IEEE International Ultrasonics Symposium*, 296–299 (2011).
9. A. K. Loya, J. P. Dumas, and T. Buma, "Photoacoustic microscopy with a tunable source based on cascaded stimulated Raman scattering in a large-mode area photonic crystal fiber," *Proc. of IEEE International Ultrasonics Symposium*, 1208–1211 (2012).
10. P. Hajireza, A. Forbrich, and R. Zemp, "In-vivo functional optical-resolution photoacoustic microscopy with stimulated Raman scattering fiber-laser source," Biomed. Opt. Express **5**(2), 539–546 (2014).
11. P. Wang, T. Ma, M. N. Slipchenko, S. Liang, J. Hui, K. K. Shung, S. Roy, M. Sturek, Q. Zhou, Z. Chen, and J.-X. Cheng, "High-speed intravascular photoacoustic imaging of lipid-laden atherosclerotic plaque enabled by a 2-kHz barium nitrite raman laser," Sci. Rep. **4**, 6889 (2014).
12. C. L. Tsai, J. C. Chen, and W. J. Wang, "Near-infrared absorption property of biological soft tissue constituents," J. Med. Biol. Eng. **21**(1), 7–14 (2001).
13. http://omlc.org/news/feb15/generic_optics/bloodSuzaki.dat
14. G. Agrawal, *Nonlinear Fiber Optics,* 4th ed. (Academic Press, 2006).
15. R. H. Stolen, C. Lee, and R. K. Jain, "Development of the stimulated Raman spectrum in single-mode silica fibers," J. Opt. Soc. Am. B **1**(4), 652–657 (1984).
16. W. Wadsworth, N. Joly, J. Knight, T. Birks, F. Biancalana, and P. Russell, "Supercontinuum and four-wave mixing with Q-switched pulses in endlessly single-mode photonic crystal fibres," Opt. Express **12**(2), 299–309 (2004).
17. Datasheet for PM980-XP fiber (Thorlabs).
18. Z. Dou, Y. Song, J. Tian, J. Liu, Z. Yu, and X. Fang, "Mode-locked ytterbium-doped fiber laser based on topological insulator: Bi_2Se_3," Opt. Express **22**(20), 24055–24061 (2014).
19. J. R. Rajian, P. L. Carson, and X. Wang, "Quantitative photoacoustic measurement of tissue optical absorption spectrum aided by an optical contrast agent," Opt. Express **17**(6), 4879–4889 (2009).

#240807 Received 11 May 2015; revised 2 Jul 2015; accepted 3 Jul 2015; published 8 Jul 2015

20. P. Hai, J. Yao, K. I. Maslov, Y. Zhou, and L. V. Wang, "Near-infrared optical-resolution photoacoustic microscopy," Opt. Lett. **39**(17), 5192–5195 (2014).
21. X. Bai, X. Gong, W. Hau, R. Lin, J. Zheng, C. Liu, C. Zeng, X. Zou, H. Zheng, and L. Song, "Intravascular optical-resolution photoacoustic tomography with a 1.1 mm diameter catheter," PLoS One **9**(3), e92463 (2014).
22. K. X. Liu and E. Garmire, "Understanding the formation of the SRS Stokes spectrum in fused silica fibers," IEEE J. Quantum Electron. **27**(4), 1022–1030 (1991).
23. G. Genty, T. Ritari, and H. Ludvigsen, "Supercontinuum generation in large mode-area microstructured fibers," Opt. Express **13**(21), 8625–8633 (2005).
24. J. Yao and L. V. Wang, "Sensitivity of photoacoustic microscopy," Photoacoustics **2**(2), 87–101 (2014).
25. Y. N. Billeh, M. Liu, and T. Buma, "Spectroscopic photoacoustic microscopy using a photonic crystal fiber supercontinuum source," Opt. Express **18**(18), 18519–18524 (2010).
26. G. Qin, M. Liao, T. Suzuki, A. Mori, and Y. Ohishi, "Widely tunable ring-cavity tellurite fiber Raman laser," Opt. Lett. **33**(17), 2014–2016 (2008).
27. G. Zhu, L. Geng, X. Zhu, L. Li, Q. Chen, R. A. Norwood, T. Manzur, and N. Peyghambarian, "Towards ten-watt-level 3-5 μm Raman lasers using tellurite fiber," Opt. Express **23**(6), 7559–7573 (2015).

1. Introduction

Photoacoustic microscopy (PAM) relies on pulsed optical excitation and acoustic detection to produce high contrast images of tissue. Optical resolution PAM (OR-PAM) achieves very fine spatial resolution by focusing the laser excitation [1]. The appropriate choice of laser wavelength is determined by the optical absorption spectrum of the tissue of interest. Short visible wavelengths (e.g. 530 to 600 nm) are used for blood oxygenation mapping [1, 2], while near-infrared wavelengths (e.g. 1200 nm) are necessary to visualize atherosclerotic plaques [3–5] or myelinated peripheral nerves [6,7].

Dye lasers and optical parametric oscillators (OPOs) are usually used for spectroscopic PAM at short visible wavelengths. OPOs are the laser of choice for tunable near-infrared operation. These lasers have high pulse energy and large wavelength tuning range, and repetition rates in the kHz range are now available. However, the very high cost of OPOs is a drawback for practical applications. We are exploring more cost-effective methods to convert a 1064 nm pulsed laser into a near-infrared multi-wavelength source suitable for spectroscopic OR-PAM of lipid-rich tissue.

Our approach uses nonlinear propagation of a laser pulse in an optical fiber to produce multiple wavelengths. A dielectric band-pass filter selects the desired wavelength for imaging. We demonstrated the first application of this technique to PAM [8,9] using a pump laser at 532 nm to produce wavelengths at 546, 560, 574, 587, and 603 nm. Hajizera used the same technique with a very high repetition rate fiber laser to perform in-vivo blood oxygenation PAM [10]. Li used a high energy 1064 nm laser to pump a barium nitrate crystal for single-wavelength PAM at 1197 nm of lipids [11]. In this paper, we use a birefringent optical fiber to produce six spectral bands between 1064 and 1325 nm for spectroscopic PAM of lipids. A unique aspect of our approach is the exploitation of fiber birefringence to produce a wavelength near the 1210 nm absorption peak of lipids (see Fig. 1(a)). Our approach is scalable to μJ pulse energies, making it a cost-effective pulsed laser for for spectroscopic OR-PAM.

2. Methods

2.1 Near-infrared multi-color pulsed laser

A schematic of our multi-color pulsed laser is shown in Fig. 1. A 1064 nm Q-switched Nd:YAG microchip laser (Teem Photonics) produces 8.2 μJ pulses with a 0.6 ns pulse duration and 7.4 kHz repetition rate. The laser pulses are coupled into 20 meters of polarization-maintaining single-mode fiber (PM-980XP, Thorlabs). The fiber coupling efficiency is approximately 40%, so the coupled peak power is estimated to be 5.5 kW. A half-wave plate adjusts the angle of the laser's linear polarization with respect to the slow axis of the fiber. The spectral properties of the optical fiber output were measured with a scanning monochromator (Optometrics) with a resolution of 4 nm. The fiber output is collimated with a 0.16 numerical aperture (NA) aspheric lens and sent through a filter wheel containing hard-coated band pass filters (Edmund Optics) at 1064, 1100, 1175, 1225, 1275, and 1325 nm. The

#240807 Received 11 May 2015; revised 2 Jul 2015; accepted 3 Jul 2015; published 8 Jul 2015

1064 nm filter has a 10 nm bandwidth and 80% transmission. All other filters have a 50 nm bandwidth and 80% transmission.

2.2 OR-PAM system

The OR-PAM system, as shown in Fig. 1(b), employs transmission-mode optical focusing and acoustic detection. The selected wavelength from the multicolor source is focused with a 0.15 NA aspheric lens. The photoacoustic signal is detected by a 25 MHz f/2 transducer (Olympus NDT). The transducer signal is amplified by 60 dB (Miteq) and sent through a 50 MHz low pass filter (Mini-Circuits) before acquisition with a digitizer board (National Instruments) operating at 250 MS/sec. Two-dimensional scanning of the object is performed with a computer controlled positioning system (Velmex). Custom-built digital electronics synchronizes the timing between the passively Q-switched laser and the motorized XY positioner. Data acquisition is performed with LabVIEW while data processing and reconstruction are performed off-line in MATLAB.

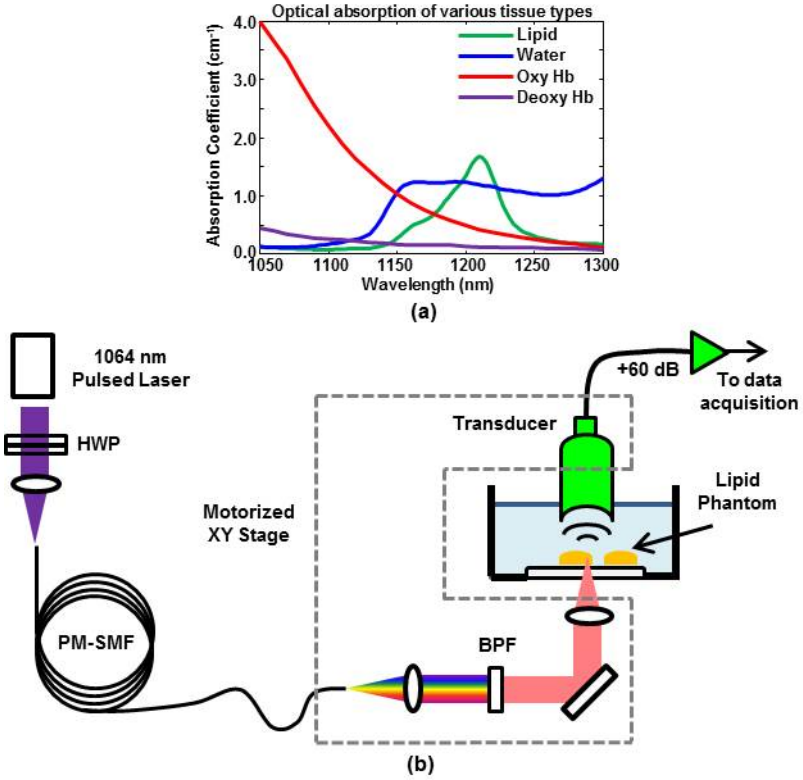

Fig. 1. (a) Optical absorption coefficient of lipid (green), water (blue), oxy-hemoglobin (red), and deoxy-hemoglobin (purple) [12, 13]. (b) Schematic of multi-color pulsed laser and optical resolution photoacoustic microscopy system. The half-wave plate (HWP) adjusts the angle of the laser polarization with respect to the slow and fast axes of the polarization-maintaining single-mode fiber (PM-SMF). A dielectric band-pass filter (BPF) selects the desired wavelength for optical resolution photoacoustic microscopy. The components within the dashed box are mounted on a motorized 2-D positioning stage.

3. Experiments and results

3.1 Optical characterization

When intense nanosecond laser pulses propagate through a single-mode optical fiber, additional wavelengths are usually produced through stimulated Raman scattering (SRS) and

#240807 Received 11 May 2015; revised 2 Jul 2015; accepted 3 Jul 2015; published 8 Jul 2015

four-wave mixing (FWM) [14,15]. SRS describes the interaction of a laser with the vibrational modes of an optical medium. FWM involves the interaction of two input waves to produce two sidebands via the nonlinear index of an optical medium. Wavelength generation may be due to a single dominant nonlinear effect or a combination, depending on a variety of input laser pulse properties and fiber characteristics. In particular, we have found that a wavelength near the 1210 nm absorption peak of lipids can be obtained by using a highly birefringent fiber and proper choice of input laser polarization.

Figure 2(a) and 2(b) correspond to the input laser polarization aligned along the slow and fast axes of the birefringent fiber, respectively. The multiple peaks of both spectra are very similar. The peak P0 (1064 nm), representing the unconverted portion of the input pump laser, is deliberately cutoff to more clearly display the remaining spectral peaks. The frequency spacing between peaks P0 (1064 nm), S1 (1117 nm), S2 (1175 nm), and S3 (1238 nm) is approximately 13.2 THz. This is consistent with cascaded SRS in fused silica, where peak P0 generates S1, then S1 generates S2, and finally S2 generates S3. The large spectral broadening of peak S3 (1238 nm) is most likely due to FWM, where two input optical waves at 1238 nm produce broad sidebands. This type of spectral broadening is commonly observed near 1300 nm, where many optical fibers have zero chromatic dispersion [16]. The absence of a distinct fourth SRS peak at 1309 nm suggests that FWM plays a more prominent role in this spectral region.

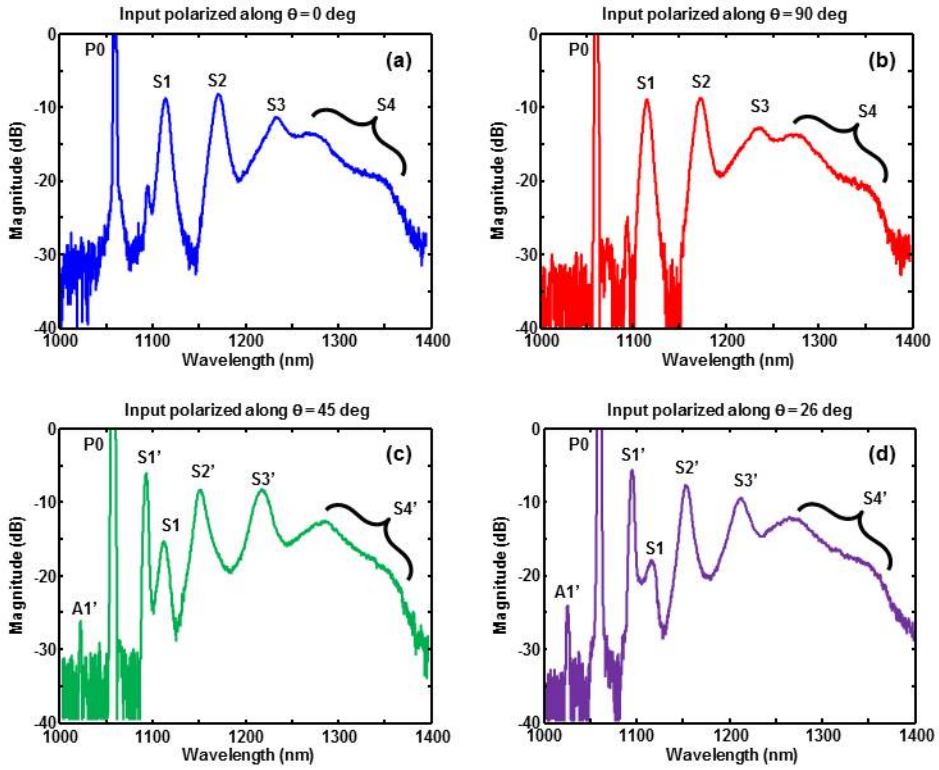

Fig. 2. Measured optical spectrum of fiber output when the input laser is polarized along (a) slow axis (b) fast axis (c) 45 degrees with respect to slow axis (d) 26 degrees with respect to slow axis.

Rotating the input laser polarization by 45 degrees significantly changes the fiber output spectrum, as shown in Fig. 2(c). The main effect is that FWM, rather than SRS, produces a very strong peak S1' (1097 nm). The presence of sideband A1' on the opposite side of P0 further supports FWM as the responsible nonlinear mechanism. Theoretically, FWM between the two polarization components of P0 produces Stokes and anti-Stokes waves along the slow

#240807 Received 11 May 2015; revised 2 Jul 2015; accepted 3 Jul 2015; published 8 Jul 2015

and fast axes of the fiber, respectively [14]. We confirmed this by placing a polarizer between the fiber output and spectrometer. The much higher amplitude of the S1' peak (compared to A1') is due to amplification by the Raman gain of fused silica.

As further evidence that S1' is due to FWM, we compared the experimental and theoretical values of the sideband frequency shift. Theoretically, the FWM sideband frequency shift is given by $f_S = \lambda_P/L_B|\beta_2|c/2\pi$, where λ_P is the pump wavelength, L_B is the fiber beat length, β_2 is the group velocity dispersion parameter of the fiber, and c is the speed of light [14]. Using typical birefringence and dispersion parameters for a polarization maintaining fiber near 1064 nm (L_B = 2.7 mm [17] and β_2 = 25.8 ps^2/km [18]), we compute a frequency shift of 8.1 THz, which is in reasonable agreement with the experimental value of 8.5 THz.

The three peaks S1' (1097 nm), S2' (1150 nm), and S3′ (1219 nm) are separated by a 13.2 THz frequency interval. Furthermore, all three peaks are polarized along the slow axis of the fiber. Both features are consistent with cascaded SRS, where S1' produces S2', and S2' produces S3′. The fairly well-defined shape of peak S3′ suggests that it is sufficiently far from the fiber's zero-dispersion wavelength to avoid excessive FWM-induced broadening. In contrast, the very broad structure of peak S4' suggests FWM in the fiber's zero-dispersion regime. Figure 2(c) does contain a weak "traditional" S1 peak (1117 nm) due to SRS, but the much stronger S1' peak dominates the wavelength generation process.

Spectra similar to Fig. 2(c) were produced for input polarization angles ranging from 22 to 48 degrees with respect to the fiber's slow axis. As shown in Fig. 2(d), the magnitude of peak S1 is minimized, but not eliminated, by adjusting the polarization angle to 26 degrees. The location of peaks S1' and S2' remain the same while peak S3′ blue-shifts slightly to 1215 nm. A slight blue shift also occurred for the broad spectral component near 1275 nm. The reasons for these blue shifts are unclear, but are most likely due to the interaction between SRS and FWM. It is worth noting that the fiber spectrum abruptly reverted to Fig. 2(a) and Fig. 2(b) when the input polarization angle was less than 22 degrees or greater than 48 degrees, respectively. The abrupt transition between the two modes of behavior is not surprising, given the threshold nature of FWM [14]. However, the asymmetry with respect to 45 degrees is still unclear and remains a subject of investigation.

Based on all four spectra shown in Fig. 2, a polarization angle of 26 degrees appears to be the most appropriate configuration for spectroscopic PAM of lipids. Many lipids have an optical absorption peak near 1210 nm [12], which is a reasonable match with peak S3′ at 1215 nm. Table 1 shows the −3 dB linewidth of each spectral peak, based on the measured spectrum from Fig. 2(d). The linewidth of the first two spectral peaks (P0 and S1') are limited

Table 1. Linewidth and pulse energy vs band-pass filter.

Spectral Peak	P0 (1064 nm)	S1' (1097 nm)	S2' (1150 nm)	S3′ (1215 nm)	Continuum	
Linewidth (nm)	4	4.5	10	20	55	–
Filter center wavelength (nm)	1064	1100	1175	1225	1275	1325
Pulse Energy (μJ)	1.17	0.25	0.39	0.48	0.43	0.20

by the spectrometer resolution (4 nm). The increasing linewidth of subsequent peaks is due to spectral broadening mentioned previously. A well-defined linewidth is not given at 1325 nm, due to the spectral continuum in this region.

The measured pulse energy after each dielectric band pass filter is also shown in Table 1. Although our available filters are not an optimal match to the actual spectral peaks, the pulse energy is 200 nJ or higher in all spectral bands, which is sufficient for in-vivo OR-PAM. The 50 nm bandwidth filters are much wider than necessary for most of the spectral peaks. This was mainly due to commercial availability of hard-coated band pass filters. Using 25 nm bandwidth filters should improve spectral sensitivity near 1215 nm without significantly

#240807 Received 11 May 2015; revised 2 Jul 2015; accepted 3 Jul 2015; published 8 Jul 2015

compromising pulse energy. However, the pulse energy at 1325 nm may become too low for in-vivo OR-PAM with our current system.

3.2 OR-PAM spatial resolution

The lateral resolution of the OR-PAM system at 1215 nm was characterized by imaging a USAF target through 1.1 mm of clear (water) and scattering (25% whole milk) media [19]. An edge of the Group 0, Element 1 pattern was imaged with an 80 x 80 pixel scan using a 2.5 μm step size. Each pixel was averaged 500 times. An edge spread function was obtained by averaging ten rows and curve fitting with a smoothing spline (smoothing parameter = 0.3) in MATLAB. The derivative of the fitted curve produced the line spread function. Lateral resolution was defined as the full width at half-maximum (FWHM) of the line spread function. As shown in Fig. 3, the lateral resolution in 1.1 mm of water and diluted milk is 6.2 μm and 8.1 μm, respectively. The same resolution analysis along the vertical dimension produced very similar results.

Axial resolution was characterized by measuring the FWHM of the envelope of the photoacoustic signal from the USAF target. Time-to-depth conversion was achieved by

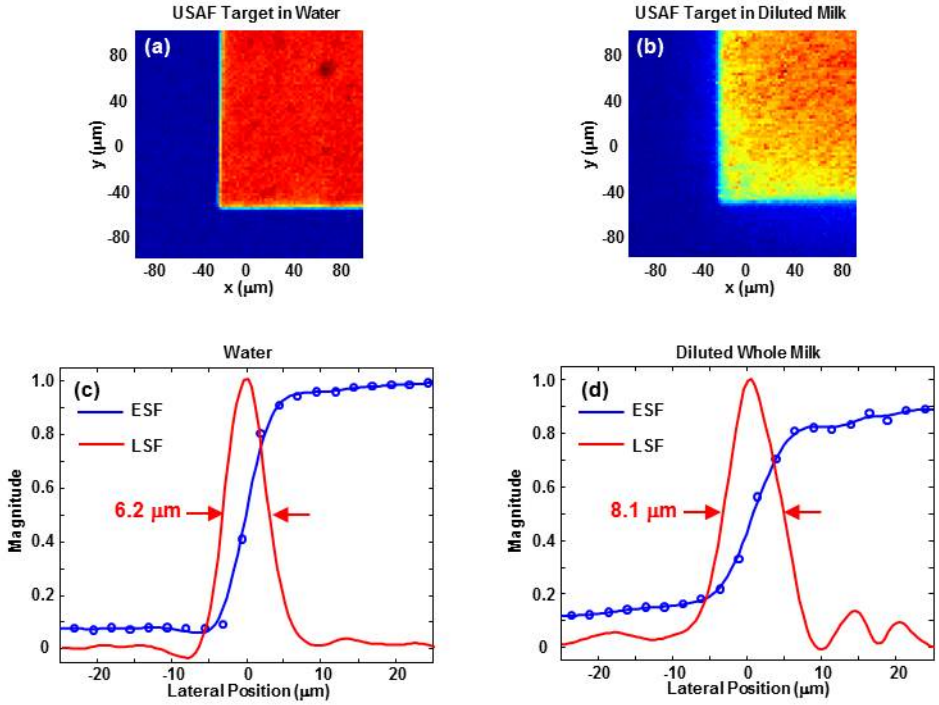

Fig. 3. OR-PAM images of a corner of the Group 0, Element 1 pattern of a USAF target immersed in 1.1 mm of (a) water and (b) 25% whole milk. Both images cover a 200 x 200 μm region and are shown over a linear scale. The horizontal edge spread function (ESF) and line spread function (LSF) in water and diluted milk are shown in (c) and (d), respectively. Both plots are centered on the edge of the chrome pattern.

measuring the shift in signal arrival time due to a 50 μm displacement of the target depth. The axial resolution was measured to be 58 μm, which is consistent with the approximately 50% fractional bandwidth (pulse-echo) of the 25 MHz receive transducer.

The sensitivity of our imaging system at 1215 nm was characterized by acquiring photoacoustic signals from a lipid phantom. The phantom consisted of a drop of butter sandwiched between 1.3 mm thick pieces of clear gelatin. The focus of the 1215 nm laser beam was positioned near the proximal surface of the butter. The laser fluence on the gelatin surface is estimated to be 0.4 mJ/cm^2, which is relatively low for OR-PAM [20,21]. The

#240807 Received 11 May 2015; revised 2 Jul 2015; accepted 3 Jul 2015; published 8 Jul 2015

signal-to-noise ratio (SNR) within a 5 – 45 MHz frequency range was obtained by computing the energy contained in the photoacoustic signal and a portion of noise. The SNR for 1, 10, 100, and 500 signal averages was found to be 3.6, 9.1, 15.7, and 25.5 dB, respectively. It is not surprising that significant signal averaging is needed to achieve an SNR greater than 20 dB, given the low surface laser fluence of our current system.

3.3 Spectroscopic OR-PAM of lipid phantoms

Spectroscopic OR-PAM was first performed on a drop of butter sandwiched between 0.9 mm thick layers of clear gelatin. The phantom was imaged with an 80 x 80 pixel scan using a 25 μm step size. The laser fluence at the gelatin surface was approximately 0.9 mJ/cm^2 at 1215 nm. 500 signal averages were acquired at each pixel in order to obtain a maximum signal-to-noise ratio (SNR) greater than 20 dB. It is worth emphasizing that a ten-fold increase in laser fluence would significantly reduce the need for signal averaging while satisfying ANSI limits at near infrared wavelengths [20].

Figure 4(a) shows the maximum amplitude projection images at 1064, 1097, 1150, 1215, 1275, and 1325 nm. All images are shown over the same linear scale. Each image was normalized based on the pulse energies in Table 1, but images were not compensated for laser energy fluctuations during data acquisition. The butter drop is clearly most prominent at 1215 nm and still visible at 1150 nm. The faint image at 1325 nm is most likely due to absorption by water contained in the clear gelatin. More specifically, photoacoustic signals are generated by the gelatin side of the gelatin-lipid interface. The pixelized nature of the low SNR images is due to the amplitude threshold for image display. The threshold was deliberately set very close to the noise floor in order to highlight the water absorption signature at 1325 nm.

Figure 4(b) shows photoacoustic spectra at three different locations within the lipid object. At each location, the spectra are averaged over a 5 x 5 pixel region. All plots are normalized

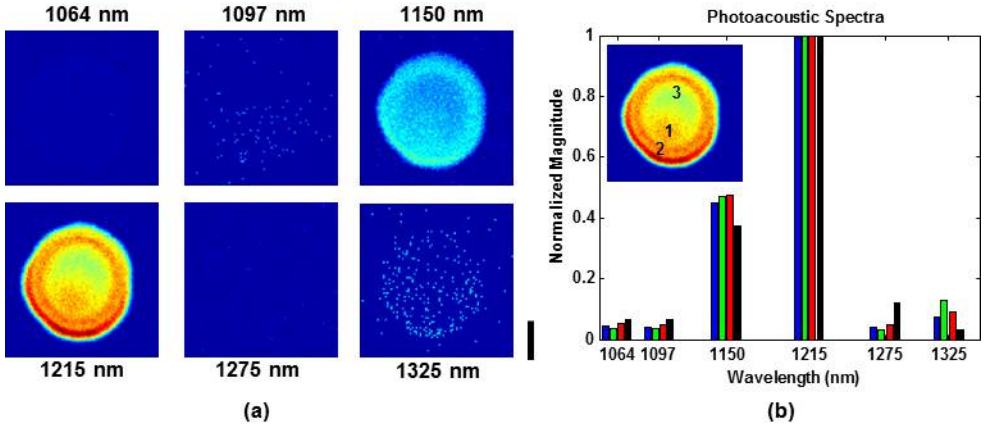

Fig. 4. Spectroscopic OR-PAM of a lipid phantom in clear gelatin. (a) Maximum amplitude projection images at 1064, 1097, 1150, 1215, 1275, and 1325 nm. The scale bar represents 500 μm. (b) Photoacoustic spectra taken at three different locations within the lipid object (see inset). Locations 1, 2, and 3 correspond to the blue, green, and red bars, respectively. Black bars are the reference spectrum based on the lipid absorption coefficient and measured laser spectrum.

#240807 Received 11 May 2015; revised 2 Jul 2015; accepted 3 Jul 2015; published 8 Jul 2015

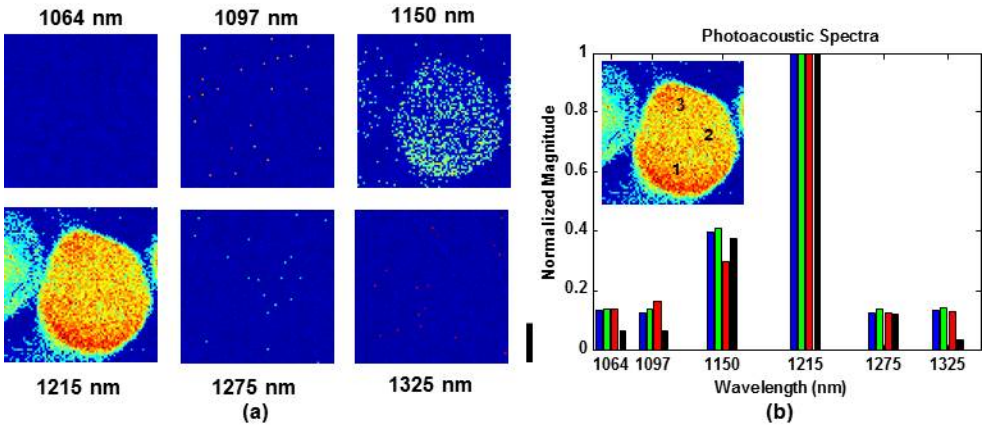

Fig. 5. Spectroscopic OR-PAM of a lipid phantom in milk + gelatin. (a) Maximum amplitude projection images at 1064, 1097, 1150, 1215, 1275, and 1325 nm. The scale bar represents 500 μm. (b) Photoacoustic spectra taken at three different locations within the central lipid object (see inset). Locations 1, 2, and 3 correspond to the blue, green, and red bars, respectively. Black bars are the reference spectrum based on the lipid absorption coefficient and measured laser spectrum.

with respect to the 1215 nm component. The spectral profiles are consistent between all three locations. For validation purposes, the photoacoustic spectra are compared to a reference spectrum computed by multiplying the lipid absorption coefficient [12] with the measured laser spectrum and integrating within the pass band of each dielectric filter. Figure 4(b) shows reasonable agreement between the photoacoustic and reference spectra.

Spectroscopic PAM was next performed on a scattering phantom consisting of three butter drops sandwiched between 0.9 mm thick layers of gelatin made with 25% diluted whole milk. Figure 5(a) shows the maximum amplitude projection images at 1064, 1097, 1150, 1215, 1275, and 1325 nm. All images are shown over the same linear scale. Each image was normalized based on the pulse energies in Table 1, but images were not compensated for laser energy fluctuations during data acquisition. The phantom was imaged with an 80 x 80 pixel scan using a 25 μm step size, and 500 signals were averaged for each pixel. The field of view is sufficient to visualize the entire central butter drop. As expected, the image SNR is worse in the milk gelatin compared to clear gelatin. However, the butter is clearly most prominent at 1215 nm and still visible in the 1150 nm image. Photoacoustic spectra at three locations within the central lipid object are shown in Fig. 5(b). Each spectrum is an average over a 5 x 5 pixel region. The overall shape of the spectral profiles is consistent with Fig. 4(b). Furthermore, the photoacoustic spectra are in reasonable agreement with the reference spectrum based on the lipid absorption coefficient and laser spectrum. The greater variability in Fig. 5(b) is most likely due to the degraded image SNR.

4. Discussion

The low pulse energy of our multi-color source requires significant signal averaging to produce adequate SNR of lipid-containing objects. A roughly ten-fold improvement is required from our system to reach the μJ pulse energies needed for practical OR-PAM applications [21]. Any strategy to increase output pulse energy must account for the inherent gain saturation in cascaded SRS [14]. A Stokes line S_m cannot grow arbitrarily large due to energy transfer to the subsequent Stokes line S_{m+1}. Therefore, increasing the fiber length tends to spread the input pump intensity over a larger number of Stokes lines. A similar saturation effect occurs if the fiber length remains constant while the input intensity is increased [22].

#240807 Received 11 May 2015; revised 2 Jul 2015; accepted 3 Jul 2015; published 8 Jul 2015

We have experimentally confirmed this saturation effect by monitoring the fiber output spectrum while varying the input pulse energy. As shown in Fig. 6, a new Stokes line was created when the coupled input pulse energy was increased by roughly 500 nJ. Furthermore, the spectral intensity of each Stokes line reaches a peak and then saturates at roughly 75% of its peak value. The maximum Stokes line energy does not correspond to the maximum input laser energy, a trend that is consistent with previous studies [10, 15]. For the particular fiber length (L = 20 m) used in our experiments, the S3′ peak (1215 nm) appears close to its peak value when the maximum input laser energy is coupled into the fiber. The S3′ peak would probably increase slightly (e.g. 10%) if a slightly longer fiber or higher input energy is used. However, saturation will most likely occur if a much longer fiber or higher input energy is used.

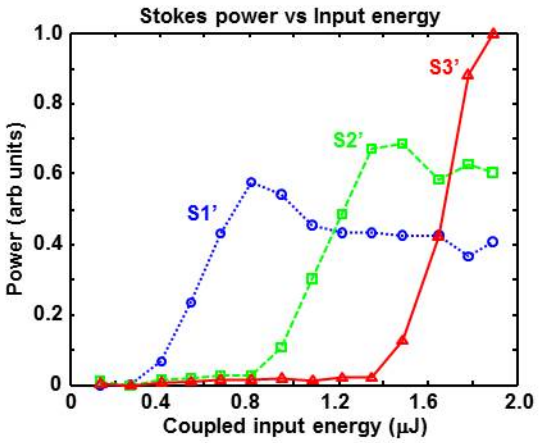

Fig. 6. Plots showing Stokes power as a function of pulse energy coupled into the optical fiber. The threshold input energies for peak S1' (blue circles), S2' (green squares), and S3′ (red triangles) occur at relatively uniform increments. Peaks S1' and S2' saturate at a value that is roughly 75% of the maximum. Peak S3′ appears to be approaching its maximum value, suggesting that L = 20 m may be slightly shorter than the ideal fiber length to maximize energy at 1215 nm.

Additional insight to increasing output pulse energy is to consider the theoretical framework for SRS. The saturation effect in SRS is related to the "critical" intensity given by $I_{cr} = 16/g_R L_{eff}$, where g_R is the Raman gain coefficient and L_{eff} is the effective fiber length [14]. The intensity in a particular Stokes line is limited by I_{cr}. Therefore, increasing the pulse energy of our multi-color source is restricted by the limitation imposed by I_{cr}. Two methods to increase pulse energy are to use: (1) a fiber with a larger core (2) a laser with longer pulse duration. Both methods allow higher energy but maintain the same intensity. The first method spreads the laser energy over a larger cross-sectional area inside the fiber, while the second method spreads energy over a larger temporal duration. The core diameter of our birefringent fiber is 5.5 μm [17]. Polarization-maintaining large mode area photonic crystal fibers (LMA-PCFs) have core diameters up to 15 μm [23]. However, a potential problem with LMA-PCFs is their relatively short zero dispersion wavelength (near 1200 nm). The onset of supercontinuum generation can prevent the generation of high energy Stokes pulses at 1200 nm.

A more straightforward approach is to use a laser with longer pulse duration. In one sense, the 0.6 ns pulse duration of our microchip laser is excessively short for our application. A sub-nanosecond pulse duration leads to two undesirable features. First, the high optical intensity inside the optical fiber leads to the SRS saturation described previously. Second, the resulting photoacoustic signals contain very high frequency components that experience severe tissue attenuation and also exceed the bandwidth of the detection transducer [24]. More conventional Q-switched lasers producing 6 to 10 ns duration pulses offer the best

#240807 Received 11 May 2015; revised 2 Jul 2015; accepted 3 Jul 2015; published 8 Jul 2015

combination of energy and bandwidth. Pulse energies exceeding 5 μJ should be easily possible, and the roughly 50 MHz photoacoustic signals are well matched to many OR-PAM detection transducers. We have not experienced any problems relating to optical damage of the fiber tip, but this may be an issue when scaling to higher laser pulse energies. Even with pulse energies of several μJ, our multi-color laser lacks the mJ energies necessary for intravascular photoacoustic (IVPA) catheters employing multimode optical fibers [4,11]. However, our multi-color laser would be very well suited for high resolution IVPA systems employing optical focusing [21].

Another practical consideration is adapting our multi-color source to a reflection-mode OR-PAM system. Systems employing high frequency delay line transducers generally require several mm of water as a coupling medium between the focusing lens and sample [1, 20]. Optical absorption in water will reduce the laser energy arriving on the sample. The optical absorption coefficient of water is approximately $\alpha = 1.3\ cm^{-1}$ at $\lambda = 1200$ nm [12]. Assuming L = 5 mm of water, the optical transmission is $\exp(-\alpha L) = 0.52$. Although not excessive, the roughly 50% optical loss must be kept in mind during system design. Similar consideration also applies to IVPA systems, where optical absorption occurs in luminal blood [3,4].

Despite the discrete wavelengths from our multi-color laser, our experimental results show that lipids can be distinguished from non-lipid objects. However, identifying specific lipid types requires closely spaced wavelengths (e.g. 1205 and 1235 nm) [3]. Continuous wavelength tuning over a roughly 20 nm range is not possible with our setup, where the generated wavelengths are constrained by the phase matching conditions (for FWM) and Raman gain (for SRS) of the optical fiber. Both factors are constrained by the fiber material properties, which can be tuned by external application of heat or pressure [14]. However, the resulting change in wavelength is extremely limited and therefore not useful for most PAM applications. Continuous tuning is possible with a supercontinuum source and a tunable optical filter [25], but this tends to produce low pulse energies (e.g. few hundred nJ).

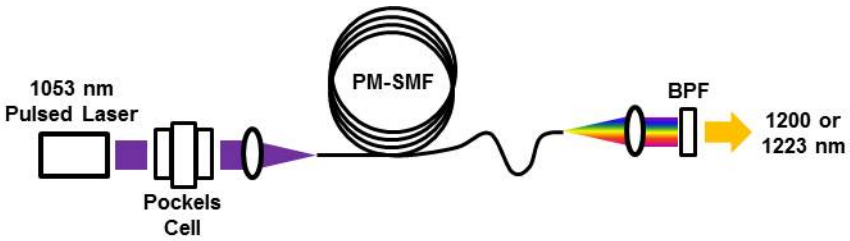

Fig. 7. Schematic of a dual-wavelength optical source to perform PAM at 1200 and 1223 nm. The 1053 nm Nd:YLF seed laser is sent through a Pockels cell, which adjust the orientation of the laser polarization with respect to the slow and fast axes of the polarization-maintaining single-mode fiber (PM-SMF). A dielectric band-pass filter (BPF) selects the desired wavelength for optical resolution photoacoustic microscopy.

A two wavelength system could be easily implemented by using an adjustable half-wave plate (e.g. Pockels cell) to control the input laser polarization with respect to the birefringent fiber's slow-axis. A potential approach is shown in Fig. 7, where a 1053 nm Nd:YLF laser is used with a Pockels cell. Laser pulses near 1223 nm (peak S3) are produced when the input laser is polarized along the fiber's slow axis. Laser pulses near 1200 nm (peak S3′) are produced when the input laser is polarized near 45 degrees. The same dielectric band-pass filter (e.g. 1190 – 1240 nm) can be used to select peak S3 (1223 nm) or S3′ (1200 nm) for intravascular OR-PAM.

Our technique can also be adapted to generate wavelengths in the 1700 nm regime, where IVPA systems target the first overtone resonance of C-H bonds in plaques [3, 4]. Unfortunately, anomalous dispersion in silica fibers causes continuum generation to dominate SRS. However, tellurite fibers have zero dispersion wavelengths beyond 2000 nm, possess large Raman gain coefficients and high damage thresholds, and have been shown to produce Raman lasers in the mid-IR range [26, 27]. Assuming a tellurite Raman shift of 22 THz [27],

#240807 Received 11 May 2015; revised 2 Jul 2015; accepted 3 Jul 2015; published 8 Jul 2015

a first-order Stokes line at 1723 nm is generated by a 1530 nm laser. This pump wavelength coincides with readily available C-band erbium doped fiber amplifiers.

Short and long term pulse stability is a potential issue for our system. Two main factors that affect stability are: (1) input laser pulse fluctuations (2) fiber misalignment. These factors will have a greater effect on the stability of higher order Stokes lines, due to the cascading nature of the wavelength generation process. Although we have not done a systematic study to characterize pulse fluctuations, preliminary observations with a photodiode and oscilloscope reveal that pulse-to-pulse fluctuations remain within 20% for all wavelengths over the course of a 12 hour period. Slight adjustments to fiber alignment are required from a week-to-week basis. A practical spectroscopic OR-PAM system will require a wavelength-calibrated photodiode to compensate the pulse-to-pulse laser fluctuations.

5. Conclusions

We have demonstrated a pulsed multi-color fiber laser source for near-infrared spectroscopic OR-PAM. Laser pulses at 1215 nm, suitable for imaging lipid-rich tissue, are possible by using a 1064 nm laser with a birefringent optical fiber. The relatively low cost and high repetition rate of our system are advantageous for practical applications. Future work in system development includes increasing the pulse energy, generating different wavelengths (e.g. using a 1053 nm seed laser), and employing a Pockels cell to rapidly select the desired wavelength for real-time two-wavelength imaging.

Acknowledgments

The authors gratefully acknowledge funding from NSF grant CBET-1157994. We thank Htoo Wai Htet, Amy Loya, and J. P. Dumas for their help with hardware and software. We also thank the reviewers for their helpful suggestions in improving this manuscript.